Computational Fluid Dynamics JOURNAL vol.8 no.2 July 1999 (pp.296–308)
Special Issue Dedicated to Professor Hisaaki Daiguji on the Occasion of His Retirement from Tohoku University
Co-Edited by Professors Mohamed Hafez and Satoru Yamamoto

A MULTI-DOMAIN METHOD FOR 3D COMPUTATION OF WAKE FLOW BEHIND A CIRCULAR CYLINDER

Yasuo OSAWA **Tayfun TEZDUYAR**

Abstract

We present a multi-domain parallel computational method for simulation of unsteady flow past a circular cylinder, including the two phases of vortex shedding in the near and far wake. The base computational method is a finite element formulation with the streamline-upwind/Petrov-Galerkin (SUPG) and pressure-stabilizing/Petrov-Galerkin (PSPG) stabilizations. The multi-domain method divides the computational domain into an ordered sequence of overlapping subdomains. The flow field computed over a leading subdomain supplies the inflow boundary conditions for the following subdomain. Meshes constructed over the second and subsequent subdomains are structured, because these subdomains do not involve any objects. In computations over these subdomains, a special-purpose implementation of the finite element formulation for structured meshes is used to obtain much higher computational speeds compared to a general-purpose implementation. 2D and 3D multi-domain computations for flow past a cylinder are carried out to capture the two phases of vortex shedding in the extended wake. The second shedding phase, where the distance between the vortices is doubled, is clearly seen in 3D computation.

1 INTRODUCTION

Recently we have developed the Multi-Domain Method (MDM) [1,2] for parallel 3D computation of the unsteady wake flow in the far downstream of an object and the influence of this wake on secondary objects located far downstream. This class of problems pose a computational challenge because the two objects are separated by a large distance compared to the length scales of the objects, and therefore unsteady flows need to be computed accurately over long wake regions. A similar computational challenge is encountered in 3D computation of a classical fluid mechanics problem: unsteady long-wake flow behind a circular cylinder. Our objective is to numerically demonstrate how the characteristics of the Karman vortex street change from the near wake of the cylinder to the far wake. Although in this case there is no secondary object far downstream, the unsteady flow behavior still needs to be computed over long wake regions, and this needs to be accomplished without exceeding the practical limits of our computational resources.

We present in this paper the MDM designed for computation of unsteady flow in near and far wakes of a circular cylinder. The base flow solver technique is a finite formulation of the Navier-Stokes equations of incompressible flows with the streamline-upwind/Petrov-Galerkin (SUPG) [3] and pressure-stabilizing/Petrov-Galerkin (PSPG) [4] stabilization. These stabilization techniques provide a finite element formulation that possesses good stability and accuracy properties even in problems with high Reynolds numbers and thin boundary layers. An important consequence of this is to be able to prevent numerical oscillations without introducing excessive numerical dissipation. These stabilization techniques also allow us to use equal-order interpolation functions for velocity and pressure without encountering the type stability problems normally encountered in using such combinations of interpolation functions.

In the MDM, the computational domain is divided into an ordered sequence of overlapping subdomains. Subdomain-1 (SD-1) is used for computation of the unsteady flow around and in the near wake of the cylinder. This subdomain is discretized with an unstructured mesh, and the computations are carried out by using a general-purpose implementation of the fi-

---

Received on April 5, 1999.

Mechanical Engineering and Materials Science
Army HPC Research Center, Rice University - MS 321
6100 Main Street, Houston, TX 77005, USA
http://www.mems.rice.edu/TAFSM/

nite element formulation. Subdomain-2, 3, ..., (SD-2, 3, ...) are used for computation of the unsteady wake flows in regions beyond the region covered by SD-1. Since these subdomains contain no objects they are discretized by using highly-refined structured meshes. This enables us to capture the long-wake flow accurately. Because the meshes used in these subdomains are structured, a special-purpose implementation of the finite element formulation based on analytical integration is used. This special-purpose implementation, with proper optimization, yields much higher computational speeds compared to the general-purpose implementation.

Even with the MDM, the spatial and temporal discretizations generate very large sets of coupled, nonlinear equations that need to be solved at every time step of the simulation. These nonlinear equation systems are solved with the Newton-Raphson iterations. In turn, at each Newton-Raphson step, an equally-large, coupled, linear equation system needs to be solved iteratively. These innermost iterations require computation of matrix-vector products. Our preferred methods for the computation of these products are the element-vector-based [5] and sparse-matrix-based [6] methods. In these iterations, we use a diagonal preconditioner, and to update the solution vector we employ the GMRES [7] search technique. These methods have been implemented on parallel computing platforms such as the CRAY T3E-900 and T3E-1200 by using the MPI programming environment. With these iterative solution strategies and parallel implementations, the MDM can be very effectively used for simulation of very large-scale, long-wake flow problems.

With the MDM, we computed two cases of flow past a circular cylinder. The first simulation, at Reynolds number (*Re*) 300, was carried out to investigate the effect of mesh refinement. Many researchers reported [8,9,10,11,12] 3D behavior behind a circular cylinder. 3D simulations in the near wake region were presented in Kalro and Tezduyar [13]. detail the 3D effects and vortex shedding in the wake as far as 30 diameters ($\bar{d}$) downstream. The second set of simulations, in 2D and 3D, were carried out at *Re*=140 to capture the wake as far as 300$\bar{d}$ downstream. Several researchers [14,15,16,17] observed a second phase of vortex shedding in the far wake. We were successful in capturing these two phases of vortex shedding with our 3D computation.

In Section 2, we review the governing equations. Brief reviews of the base finite element formulation and MDM are presented in Sections 3 and 4. The numerical results from the investigation of the effect of mesh refinement at *Re*=300 is presented in Section 5. In Section 6, we present the results from the case at *Re*=140, and with the simulation domain extending as far downstream as 300$\bar{d}$. The concluding remarks are provided in Section 7.

2 GOVERNING EQUATIONS

The Navier-Stokes equations of incompressible flows for domain Ω with boundary Γ are written as

$$\rho\left(\frac{\partial \boldsymbol{u}}{\partial t} + \boldsymbol{u}\cdot\nabla\boldsymbol{u} - \boldsymbol{f}\right) - \nabla\cdot\boldsymbol{\sigma} = 0 \quad \text{on } \Omega \quad (1)$$

$$\nabla\cdot\boldsymbol{u} = 0 \quad \text{on } \Omega \quad (2)$$

where ρ, $\boldsymbol{u}$ and $\boldsymbol{f}$ are the density, velocity and the external force, respectively. The stress tensor $\boldsymbol{\sigma}$ is defined as

$$\boldsymbol{\sigma}(p,\boldsymbol{u}) = -p\boldsymbol{I} + 2\mu\boldsymbol{\varepsilon}(\boldsymbol{u}). \quad (3)$$

Here p, $\boldsymbol{I}$ and μ are the pressure, identity tensor and the viscosity, respectively. The strain rate tensor $\boldsymbol{\varepsilon}(\boldsymbol{u})$ is defined as

$$\boldsymbol{\varepsilon}(\boldsymbol{u}) = \frac{1}{2}\left((\nabla\boldsymbol{u}) + (\nabla\boldsymbol{u})^T\right). \quad (4)$$

Both Dirichlet- and Neumann-type boundary conditions are accounted for:

$$\begin{aligned} \boldsymbol{u} &= \boldsymbol{g} \quad \text{on} \quad \Gamma_g, \\ \boldsymbol{n}\cdot\boldsymbol{\sigma} &= \boldsymbol{h} \quad \text{on} \quad \Gamma_h. \end{aligned} \quad (5)$$

Here Γ_g and Γ_h are complementary subsets of the boundary Γ, $\boldsymbol{n}$ is the unit normal vector, and $\boldsymbol{g}$ and $\boldsymbol{h}$ are specified functions. A divergence-free velocity field is specified as the initial condition.

3 FINITE ELEMENT FORMULATION WITH STABILIZATION

The domain Ω is discretized into sub-domains Ω_e, $e = 1, 2, \cdots, n_{el}$, where n_{el} is the number of elements. We define the finite element interpolation function spaces $\mathcal{S}^h_{\boldsymbol{u}}$ for velocity and $\mathcal{S}^h_p$ for pressure, and the corresponding test function spaces $\mathcal{V}^h_{\boldsymbol{u}}$ and $\mathcal{V}^h_p$:

$$\mathcal{S}^h_{\boldsymbol{u}} = \left\{\boldsymbol{u}^h | \boldsymbol{u}^h \in \left[H^{1h}(\Omega)\right]^{n_{sd}}, \quad \boldsymbol{u}^h = \boldsymbol{g}^h \quad \text{on} \quad \Gamma_g\right\}, \quad (6)$$

$$\mathcal{V}^h_{\boldsymbol{u}} = \left\{\boldsymbol{w}^h | \boldsymbol{w}^h \in \left[H^{1h}(\Omega)\right]^{n_{sd}}, \quad \boldsymbol{w}^h = 0 \quad \text{on} \quad \Gamma_g\right\}, \quad (7)$$

$$\mathcal{S}^h_p = \mathcal{V}^h_p = \left\{q^h | q^h \in H^{1h}(\Omega)\right\}. \quad (8)$$

Here $H^{1h}(\Omega)$ is the finite-dimensional function space over Ω. The stabilized finite element formulation is written as follows: find $\boldsymbol{u}^h \in \mathcal{S}^h_{\boldsymbol{u}}$ and $p^h \in \mathcal{S}^h_p$ such that $\forall \boldsymbol{w}^h \in \mathcal{V}^h_{\boldsymbol{u}}$ and $q^h \in \mathcal{V}^h_{\boldsymbol{u}}$:

$$
\begin{aligned}
&\int_{\Omega} \boldsymbol{w}^h \cdot \rho \left(\frac{\partial \boldsymbol{u}^h}{\partial t} + \boldsymbol{u}^h \cdot \nabla \boldsymbol{u}^h - \boldsymbol{f} \right) \mathrm{d}\,\Omega \\
&\quad + \int_{\Omega} \boldsymbol{\varepsilon}(\boldsymbol{w}^h) : \boldsymbol{\sigma}(p^h, \boldsymbol{u}^h)\,\mathrm{d}\,Q \\
&\quad + \int_{\Omega} q^h \nabla \cdot \boldsymbol{u}^h \,\mathrm{d}\,Q \\
&\quad + \sum_{e=1}^{n_{el}} \int_{\Omega^e} \frac{1}{\rho} \left[\tau_{SUPG}\, \rho \boldsymbol{u}^h \cdot \nabla \boldsymbol{w}^h + \tau_{PSPG}\, \nabla q^h \right] \cdot \\
&\quad\ \left[\rho \left(\frac{\partial \boldsymbol{u}^h}{\partial t} + \boldsymbol{u}^h \cdot \nabla \boldsymbol{u}^h \right) - \nabla \cdot \boldsymbol{\sigma}(p^h, \boldsymbol{u}^h) - \rho \boldsymbol{f} \right] \mathrm{d}\,\Omega^e \\
&\quad + \sum_{e=1}^{n_{el}} \int_{\Omega^e} \delta \nabla \cdot \boldsymbol{w}^h \rho \nabla \cdot \boldsymbol{u}^h \,\mathrm{d}\,\Omega^e \\
&= \int_{\Gamma_h} \boldsymbol{w}^h \cdot \boldsymbol{h}^h \,\mathrm{d}\,\Gamma. \qquad (9)
\end{aligned}
$$

For further details on the formulation see Tezduyar [4].

4 THE MULTI-DOMAIN METHOD

The full simulation domain is divided into an ordered sequence of overlapping subdomains.

SD-1 is used for computation of the unsteady flow around the cylinder and in its near wake. The inflow boundary conditions for this subdomain are the free-stream conditions. This subdomain is discretized using an unstructured mesh. A general-purpose implementation of the finite element formulation is used for computations in this subdomain. An appropriately positioned "outflow layer" is selected in this subdomain, downstream of the cylinder. This outflow layer is used for extracting flow data at every time step.

SD-2, 3, ..., are used for computation of the unsteady flow in the wake regions further downstream. These subdomains would typically be much longer than SD-1. Since SD-2, 3, ..., contain no objects, they are discretized by highly-refined structured meshes. A special-purpose implementation of the finite element formulation for structured grids is used in these subdomains. This special-purpose, optimized implementation is based on analytical integration over finite element domains, and enables us to compute at higher speeds compared to what we can get with the general-purpose implementation. Furthermore, the computations over these subdomains can also be accomplished by methods other than the finite element method. For example, a spectral method might be more desirable for computations with very regular geometries.

The time-dependent boundary conditions at the inflow layer of SD-2 are obtained by parallel projection from the outflow layer of SD-1. The inflow layer of SD-2 overlaps with outflow layer of SD-1. In obtaining the results reported in this paper, we specify the velocity and pressure at the first plane of the inflow layer, and the velocity at the second plane. As we did for SD-1, we select a suitably located outflow layer in SD-2.

The computation for downstream subdomains, such as SD-3, 4, ..., are carried out in a fashion similar to what we had for SD-2. We note that the computations over these different subdomains can be performed on different computational platforms and essentially in parallel, provided a leading subdomain is at least one time step ahead of the following subdomain. This parallelism is in addition to the one we have within individual subdomains.

For further details on the MDM see [2].

5 CYLINDER WAKE COMPUTATION AT *Re* = 300: EFFECT OF MESH REFINEMENT

We computed this problem first with the single-domain and then with the multi-domain method.

In the single-domain computation we used the same mesh as the one used by Kalro and Tezduyar [13]. In the multi-domain computation we used a highly-refined structured mesh (see Fig.1). The diameter of the cylinder is 2 units, and the span length is 8 units. The center of the cylinder is located at the origin of the computational domain. The upstream, downstream, and crossflow (i.e. top and bottom lateral) boundaries are located, respectively, at 15, 60 ($30\overline{d}$) and 15 units from the origin (see Fig.1). The mesh consists of 197,948 nodes and 186,240 hexahedral elements, and results in 760,107 equations. The boundary conditions consist of uniform inflow velocity, zero-shear stress and zero-normal velocity at lateral boundaries, traction-free condition at the outflow boundary, and no-slip condition on the cylinder. The outflow layer is selected in such a way that its upstream plane is located 4 units downstream of the origin.

In the multi-domain computation, the wake subdomain (SD-2) stretches 56, 8 and 30 units along the streamwise, spanwise, and crossflow directions, respectively. SD-2 mesh consists of 1,163,565 nodes and 1,126,400 hexahedral elements, and results in 4,553,457 equations. Compared to the wake region of the single-domain model, the number of elements in SD-2 is around 3.3 and 1.8 times larger in the streamwise and crossflow directions, and 2.0 times larger in the spanwise direction. The inflow boundary conditions are extracted by projection from the solution ob-

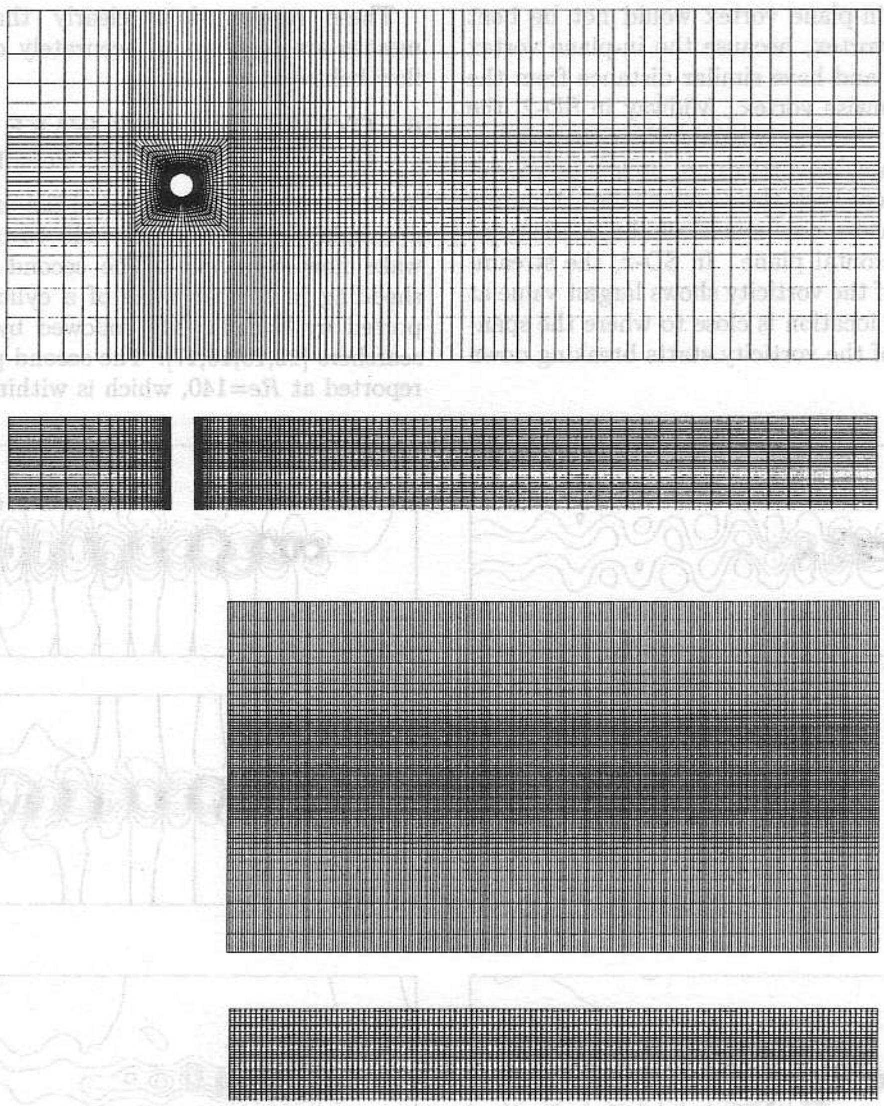

Fig.1: Cylinder wake computation at Re=300: effect of mesh refinement. Mesh for the single-domain computation (upper) and for the multi-domain computation (lower). For visual clarity, the bottom frame shows a diluted version of the actual mesh, coarsened by a factor of 2 in the spanwise direction.

tained in the single-domain computation. Boundary conditions similar to those for the single-domain computation are imposed at the lateral and downstream boundaries. For the purpose of clarity, the bottom image in Fig.1 shows a mesh coarsened by a factor of 2 in the spanwise direction.

The free-stream velocity is 1.0, and the time step size is 0.1. The number of nonlinear iterations per time step is 2. In the GMRES update, the size of the Krylov space is 10, without restart. These computations were carried out on a CRAY T3E-900. The computation, per time step, requires 26 seconds on 32 processors for the single-domain computation, and 26 seconds on 48 processors for SD-2.

Figure 2 shows the velocity and pressure for both computations. Figure 3 shows the vorticity iso-surfaces from these computations. These figures clearly show that the solution on SD-2 captures the flow features in greater detail, and maintains these features all the way to the outflow boundary. The spanwise vorticity iso-surfaces corresponding to the Karman vortex are almost straight in vertical direction in the near wake. The in-plane vortices form arch shapes in horizontal planes. These two types of vortices interact with each other. The spanwise vortex would be bent by the in-plane vortex. On the other hand, the in-plane vortex would not be bent by the spanwise vortex, because the in-plane vortex is already curved and have similar distance from the center of the spanwise vortex. Midway in SD-2, the spanwise vortices become twisted. Near the outflow boundary, the spanwise vortices are broken down, yet the in-plane vortices keep their arch shapes. Figure 4 shows the streamwise component of the vorticity at the centered horizontal plane. In SD-2, the streamwise component of the vorticity shows largest value at around $23\overline{d}$. This location is close to where the spanwise component of the vorticity starts breaking down in Fig.3.

These results show clearly that highly-refined meshes are required to accurately capture the wake flow behavior.

6 CYLINDER LONG-WAKE COMPUTATION AT $Re = 140$

With the MDM, we computed the unsteady flow past a circular cylinder at Re=140 to capture the long-wake flow behavior. The second phase of vortex shedding in the far wake of a cylinder was first reported by Taneda [14], followed by many other researchers [12,15,16,17]. The second phase shedding is reported at Re=140, which is within laminar regime.

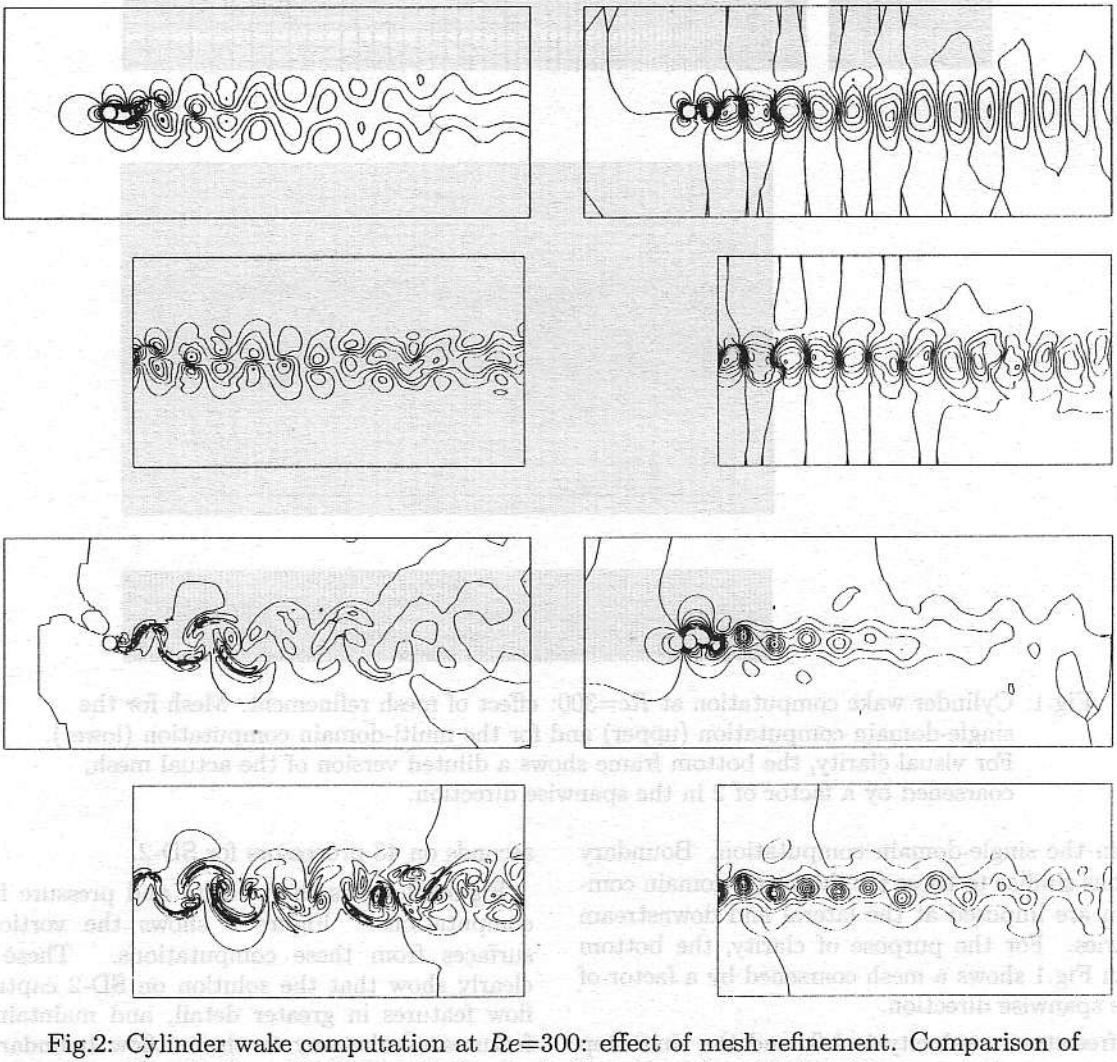

Fig.2: Cylinder wake computation at Re=300: effect of mesh refinement. Comparison of the solutions obtained with the single-domain and multi-domain computations; streamwise component of the velocity (upper-left), crossflow component of the velocity (upper-right), spanwise component of the velocity (lower-left), and pressure (lower-right).

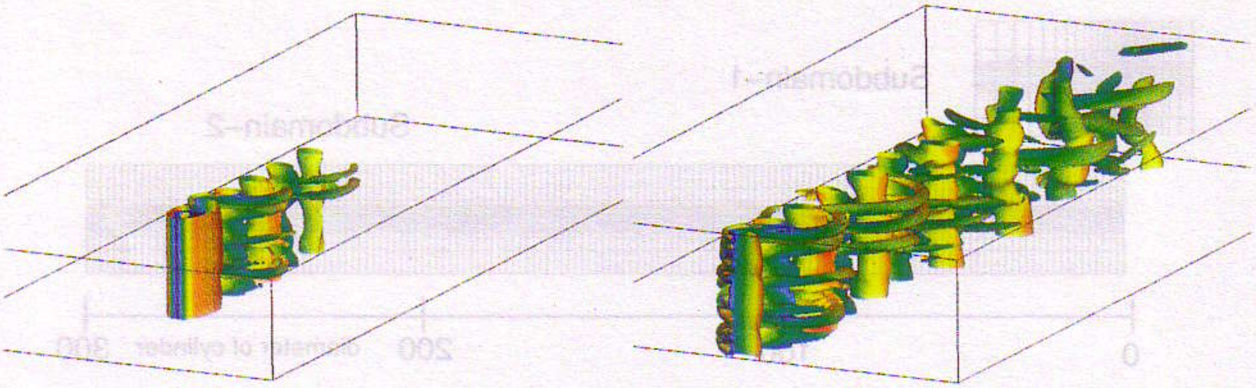

Fig.3: Cylinder wake computation at Re=300: effect of mesh refinement. Vorticity iso-surfaces corresponding to 0.6 value, obtained with the single-domain computation (left), and the multi-domain computation (right).

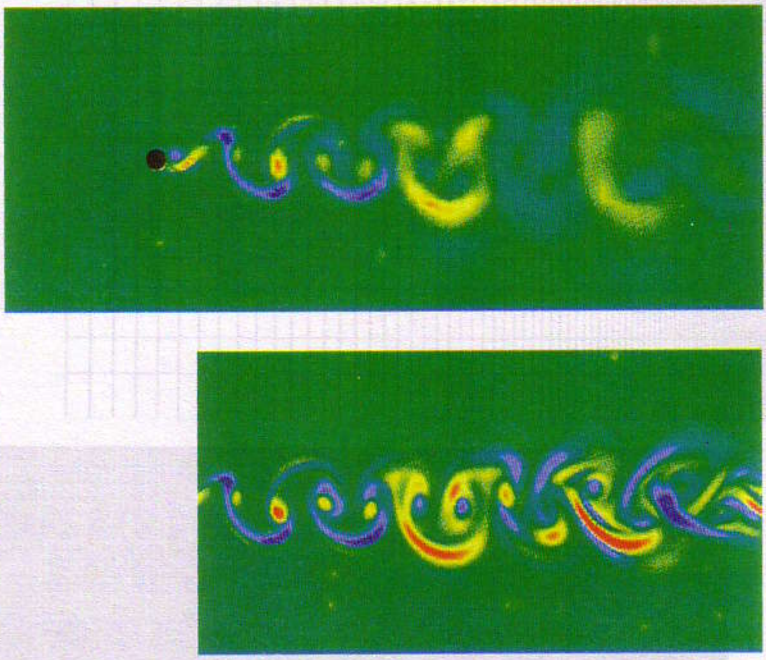

Fig.4: Cylinder wake computation at Re=300: effect of mesh refinement. The streamwise component of vorticity at the centered horizontal plane, obtained with the single-domain computation (upper), and the multi-domain computation (lower).

Cimbala [16] attributes this behavior to hydrodynamic instability, while Williamson [12] suggests that this is caused by the sensitivity of the wake to small-scale perturbations. 3D numerical simulation of this problem is not an easy task because of its long-wake domain extending to 300$\overline{d}$ downstream.

First a 2D simulation was performed. The entire domain was divided into two subdomains: one around the cylinder, and the other one in the wake domain, starting at 2$\overline{d}$ downstream from the center of the cylinder and extending to 300$\overline{d}$ (see Fig.5). Both subdomains have one element in the spanwise direction.

The first subdomain (SD-1) contains the cylinder, located at the origin of the computational domain. The radius and the span length are both one unit. The upstream, downstream, and crossflow boundaries are located, respectively, at 15, 60 and 20 units from the origin (see Fig.6). SD-1 mesh consists of 16,432 nodes and 8,000 hexahedral elements, and results in 48,188 equations. The same boundary conditions as

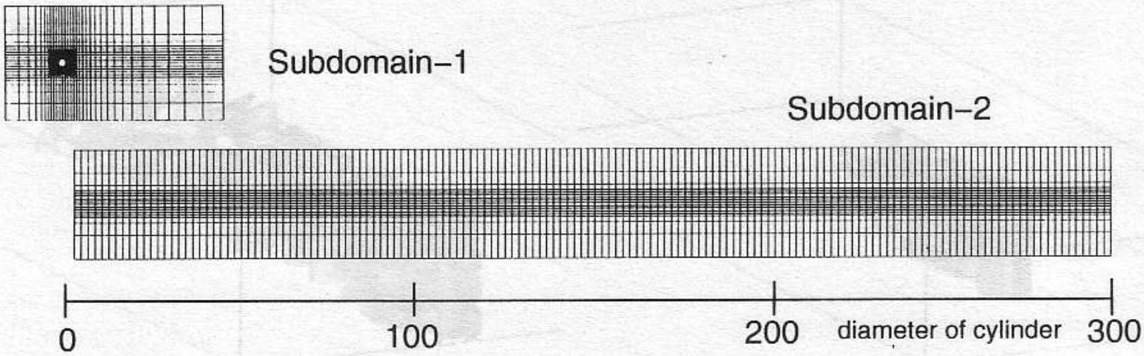

Fig.5: 2D cylinder long-wake computation at $Re = 140$. Arrangement of the two subdomains. Frames do not show the actual meshes.

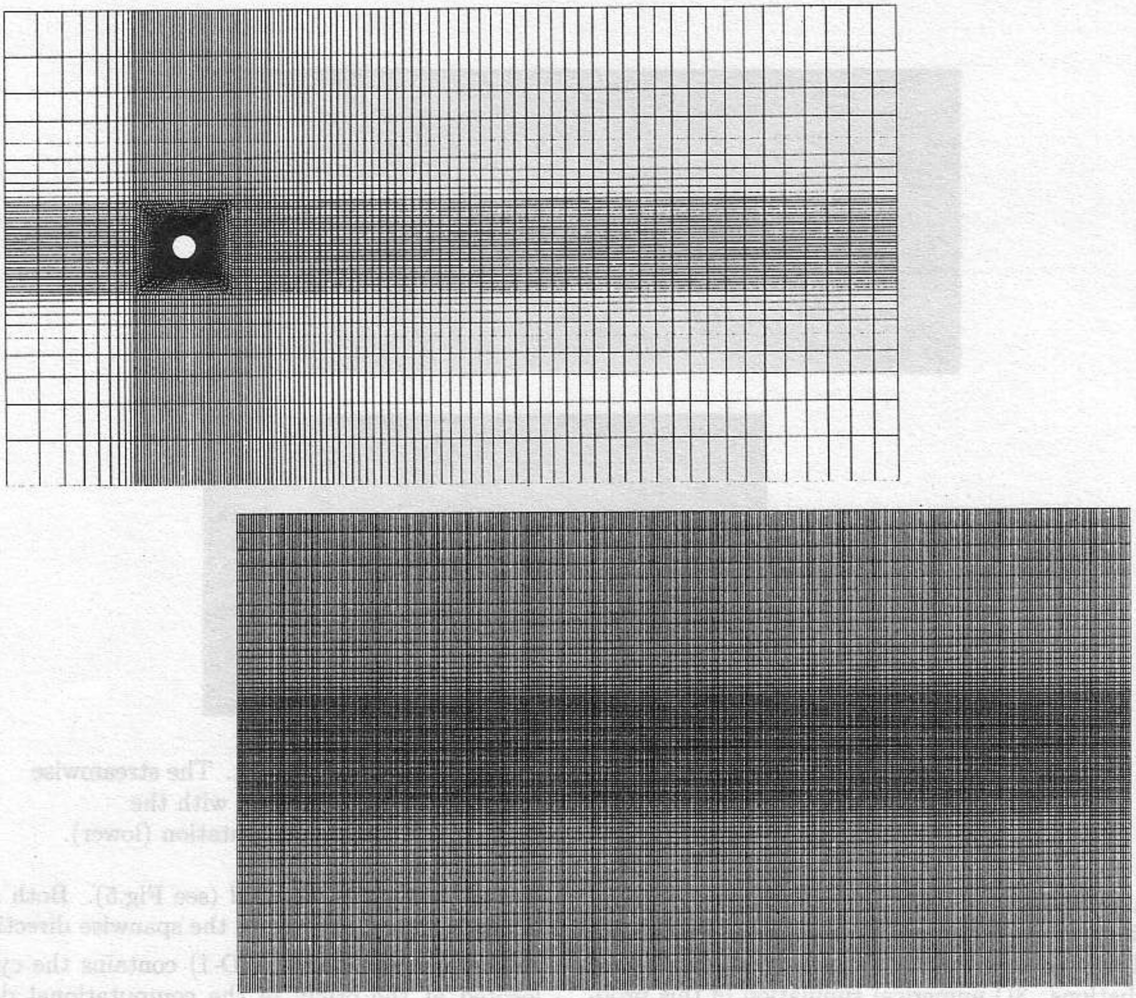

Fig.6: 2D cylinder long-wake computation at $Re = 140$. Mesh for Subdomain-1 (upper), and for the upstream 1/8 of Subdomain-2 (lower). For visual clarity, the lower image shows a diluted version of the actual mesh, coarsened by a factor of 2 in the streamwise and crossflow directions.

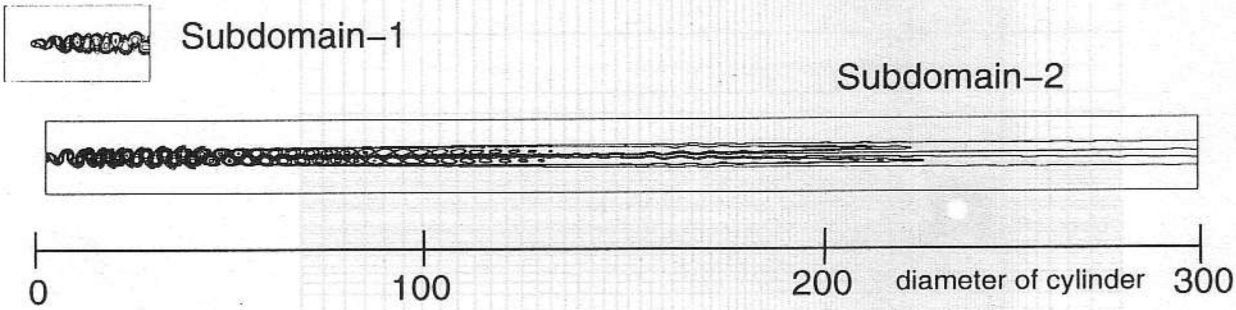

Fig.7: 2D cylinder long-wake computation at $Re = 140$. Magnitude of the vorticity for Subdomain-1 (upper) and Subdomain-2 (lower).

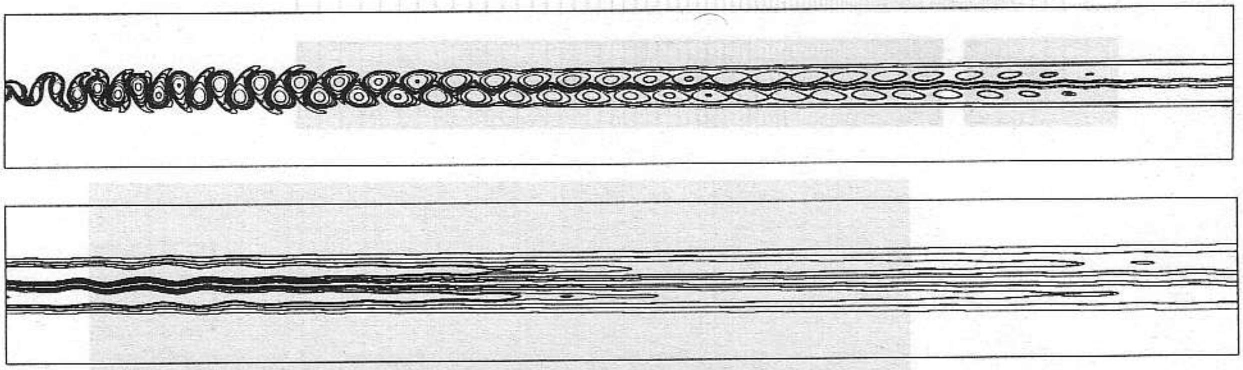

Fig.8: 2D cylinder long-wake computation at $Re = 140$. Magnitude of the vorticity for the upstream half of Subdomain-2 (upper) and downstream half of Subdomain-2 (with smaller magnitude of contours) (lower).

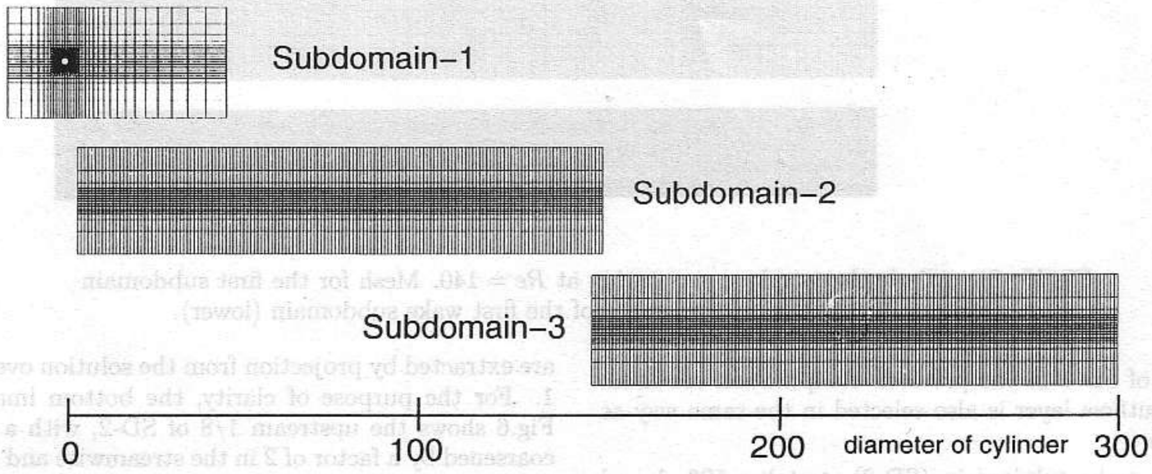

Fig.9: 3D cylinder long-wake computation at $Re = 140$. Arrangement of the three subdomains. Frames do not show the actual meshes.

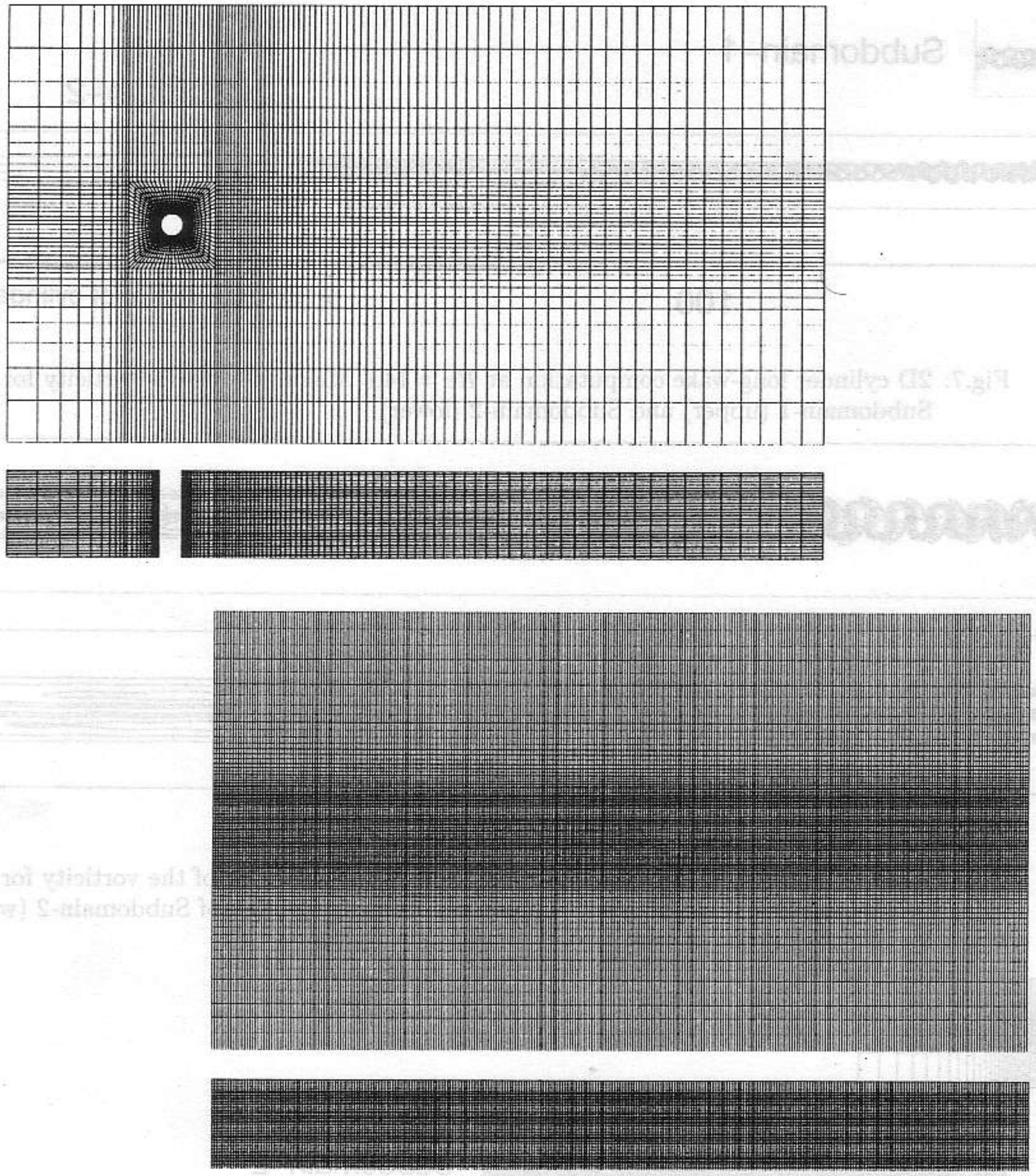

Fig.10: 3D cylinder long-wake computation at $Re = 140$. Mesh for the first subdomain (upper), and for the upstream 1/4 of the first wake subdomain (lower).

those of SD-1 in the previous computation are used. The outflow layer is also selected in the same way as before.

The wake subdomain (SD-2) stretches 596, 1 and 40 units along the streamwise, spanwise, and cross-flow directions, respectively. SD-2 mesh consists of 1,824,066 nodes and 905,920 hexahedral elements, resulting in 5,446,832 equations. Boundary conditions similar to those for SD-1 are imposed at the lateral and downstream boundaries. The inflow conditions are extracted by projection from the solution over SD-1. For the purpose of clarity, the bottom image in Fig.6 shows the upstream 1/8 of SD-2, with a mesh coarsened by a factor of 2 in the streamwise and cross-flow directions.

The free-stream velocity is 1.0 and the time step size is 0.1. The number of nonlinear iterations per time step is 2. In the GMRES update, the size of the Krylov space is 20, without restart. These computations were carried out on a CRAY T3E-1200. The computation, per time step, requires 1.9 seconds on 16 processors

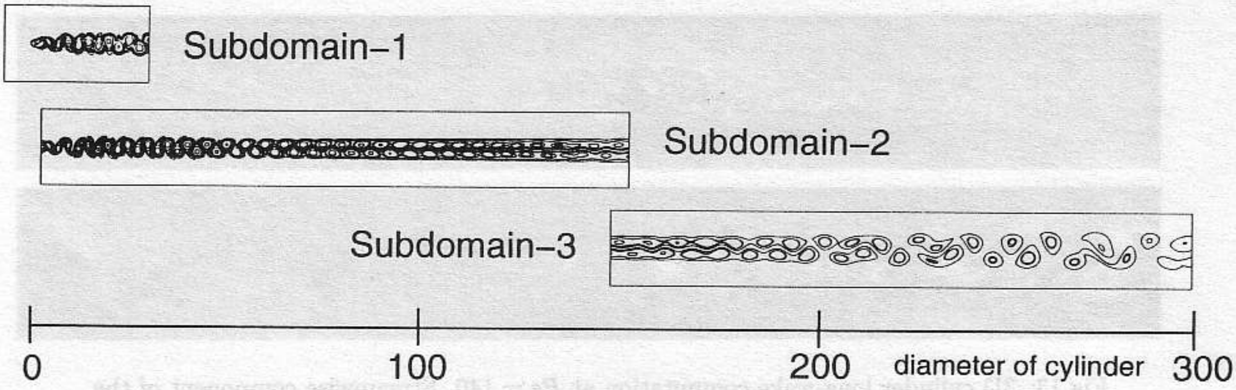

Fig.11: 3D cylinder long-wake computation at $Re = 140$. Magnitude of the vorticity for Subdomain-1 (upper), Subdomain-2 (middle), and Subdomain-3 (lower).

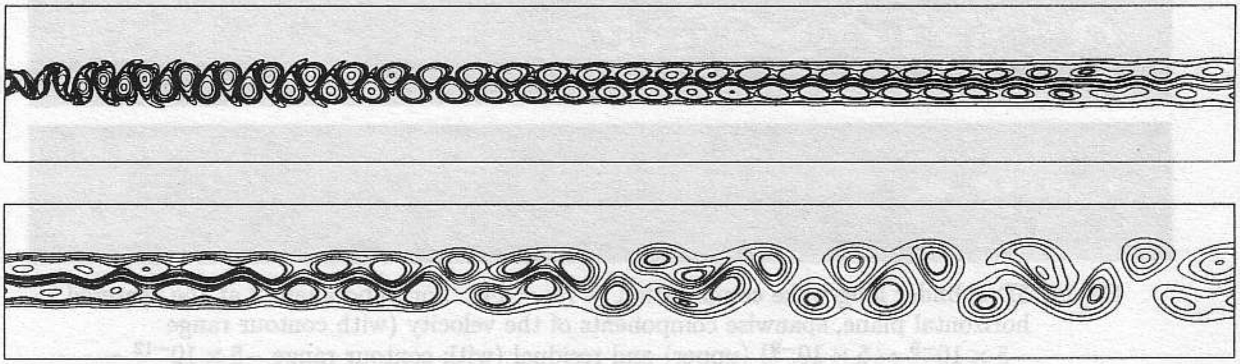

Fig.12: 3D cylinder long-wake computation at $Re = 140$. Magnitude of the vorticity for Subdomain-2 (upper) and Subdomain-3 (with smaller magnitude of contours) (lower).

for SD-1, and 26 seconds on 48 processors for SD-2.

Figure 7 shows the magnitude of the vorticity in these computations. Figure 8 shows the magnitude of the vorticity for the upstream and downstream halves of SD-2. We note that, because of the highly-refined mesh, the solution over SD-2 captures vortices which are much clearer in the near wake. No second phase vortex shedding is observed in the far wake, though the Karman vortex street is captured in the near wake. From laboratory experiments [15,16], the transition between these two phases is expected at $100\overline{d} \sim 150\overline{d}$. However in our simulation, vorticity decays in that region (see Fig.7). This leads us to think that the 3D effects are the cause of the second phase vortex shedding.

We also computed this problem in 3D, but with three subdomains: first one around the cylinder; second one starting at $2\overline{d}$ downstream from the center of the cylinder and extending to $155\overline{d}$; and the third one starting at $150\overline{d}$ and extending to $300\overline{d}$ (see Fig.9).

The first subdomain (SD-1) has the same boundary conditions and in-plane domain size as those of SD-1 in 2D computations. The difference is that the span length of the cylinder is 8 units. SD-1 mesh consists of 213,856 nodes and 201,600 hexahedral elements, and results in 822,479 equations (see Fig.10).

The upstream wake subdomain (SD-2) stretches 306, 8 and 40 units along the streamwise, spanwise and crossflow directions, respectively. SD-2 mesh consists of 4,470,025 nodes and 4,308,480 hexahedral elements, and results in 17,536,577 equations. The inflow conditions are obtained by projection from the solution over SD-1. Boundary conditions similar to those for SD-1 are imposed at the lateral and downstream boundaries. The inflow layer is selected in such a way that its upstream plane is located 300 units downstream of the origin (10 units upstream of the outflow boundary). For the purpose of clarity, SD-2 mesh in Fig.10

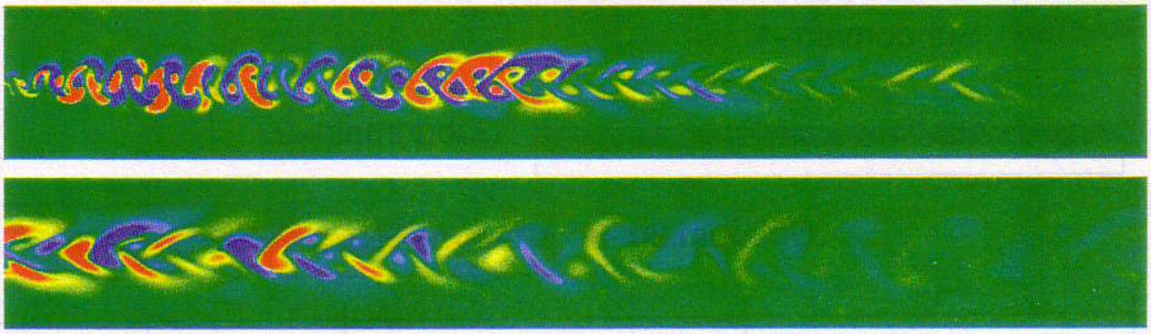

Fig.13: 3D cylinder long-wake computation at $Re = 140$. Streamwise component of the vorticity at the centered horizontal plane, shown for Subdomain-2 (upper) and Subdomain-3 (lower).

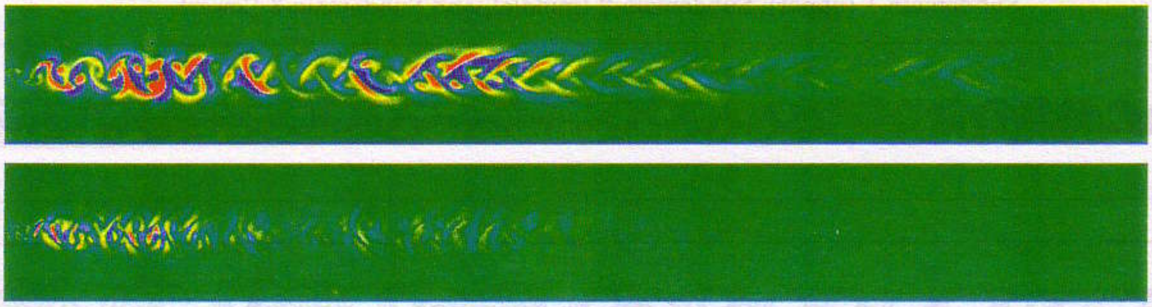

Fig.14: 3D cylinder long-wake computation at $Re = 140$. For Subdomain-2 at the centered horizontal plane, spanwise components of the velocity (with contour range $-5 \times 10^{-9} \sim 5 \times 10^{-9}$) (upper) and residual (with contour range $-5 \times 10^{-12} \sim 5 \times 10^{-12}$) (lower).

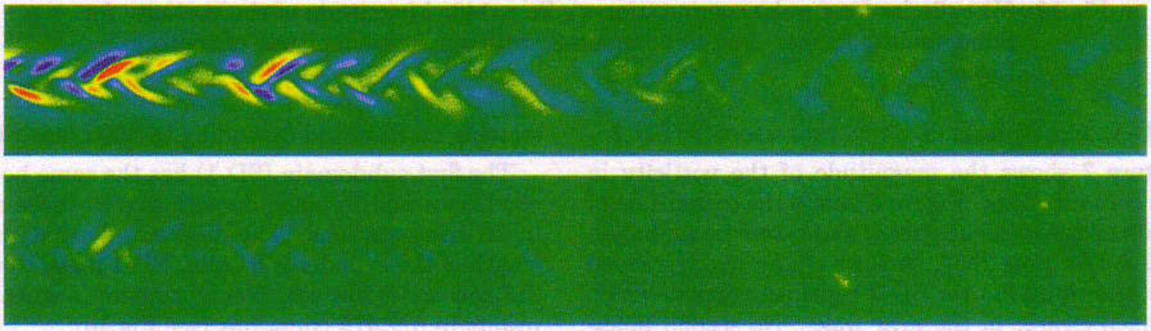

Fig.15: 3D cylinder long-wake computation at $Re = 140$. For Subdomain-3 at the centered horizontal plane, spanwise components of the velocity (with contour range $-5 \times 10^{-11} \sim 5 \times 10^{-11}$) (upper) and residual (with contour range $-5 \times 10^{-14} \sim 5 \times 10^{-14}$) (lower).

shows the upstream 1/4 of the SD-2.

The downstream wake subdomain (SD-3) stretches 300, 8 and 40 units along the streamwise, spanwise, and crossflow directions, respectively. The mesh density in SD-3 is the same as what we have in SD-2. SD-3 mesh consists of 4,382,449 nodes and 4,224,000 hexahedral elements, and results in 17,192,513 equations. The inflow conditions are obtained by projection from the solution over SD-2. Boundary conditions similar to those for SD-2 are imposed at the lateral and downstream boundaries.

The free-stream velocity is 1.0 and the time step size is 0.1. The number of nonlinear iterations per time step is 2. In the GMRES update, the size of the Krylov space is 20, without restart. Only for SD-3 computation, the number of nonlinear iterations per time step is three. These computations were carried out on a CRAY T3E-1200. The computation, per time step, requires 9 seconds on 64 processors for SD-1, 35 and 51 seconds on 128 processors for SD-2 and SD-3, respectively.

Figure 11 shows the magnitude of the vorticity at the centered horizontal plane in these computations. Figure 12 shows close-up view of the magnitude of the vorticity at the centered horizontal plane in SD-2 and SD-3. SD-2 captures the transition of vortex shedding near the outflow boundary, in addition to the Karman vortex street in the near wake. SD-3 successfully captures the second phase of vortex shedding. The spacing between the vortices in the second phase of vortex shedding is about twice as large compared to the spacing we see in the first phase. Fig.13 shows, at the centered horizontal plane, the streamwise component of the vorticity in SD-2 and SD-3. In SD-2, the pattern of the in-plane vortices is similar to the those seen at Re=300.

The magnitude of the streamwise vortices in these subdomains is very small, such as 5×10^{-9} and 5×10^{-11}, respectively. We compared at the same plane the spanwise components of the velocity and residual to confirm the true existence of these vortices. This component of the velocity creates the streamwise vorticity and 3D effects. In Figs.14 and 15, we compare, at the centered horizontal plane, the spanwise components of the velocity and residual in SD-2 and SD-3. The residual is much smaller than the velocity. For SD-2, the maximum contour value for the velocity is 5×10^{-9}, and 5×10^{-12} for the residual. For SD-3, the numbers are 5×10^{-11} for the velocity 5×10^{-14} for the residual. These observations imply that the spanwise velocity component we see is real, and not numerical error. From these verifications, we can conclude that the streamwise vorticity component we see is also real.

From these results, we confirm the existence of streamwise vortices, which is a 3D behavior, for Reynolds numbers even as small as 140. The magnitude of these vortices is much smaller compared to the other components of the vorticity. The shapes of these vortices at the centered horizontal plane are similar to those in higher Reynolds number (such as 300) flows. Comparison of 2D and 3D computations suggests that the in-plane vortices play an important role in producing the second phase of vortex shedding in far downstream. From these observations, we can conclude that the second phase of vortex shedding is generated by very small 3D effects.

7 CONCLUDING REMARKS

With our multi-domain parallel computational method, we were able to capture the details of unsteady wake flow behind a circular cylinder. At Reynolds number 300 we show that the wake exhibits strong 3D behavior. This 3D behavior includes in-plane vortices breaking the spanwise (Karman) vortices. We also show that this class of flows involve 3D effects for cases with Reynolds numbers as low as 140. For Reynolds number 140 we also show that at far downstream the distance between the vortices approximately doubles, and a second phase of vortex shedding is generated.

Acknowledgment

The work reported in this paper was partially sponsored by NASA JSC (grant no. NAG9-1059), AFOSR (contract no. F49620-98-1-0214), and by the AHPCRC under the auspices of the Department of the Army, ARL cooperative agreement no. DAAH04-95-2-0003 and contract no. DAAH04-95-C-0008. The content does not necessarily reflect the position or the policy of the government, and no official endorsement should be inferred. The first author has been supported by the Bridgestone Corp. We are grateful to Dr. Vinay Kalro for valuable discussions.

REFERENCES

[1] Y. Osawa, V. Kalro and T.E. Tezduyar: Multi-domain parallel computation of wake flows around secondary objects; Proc. 4th Japan-US Symp. Finite Element Methods in Large-Scale CFD, 1998

[2] Y. Osawa, V. Kalro and T.E. Tezduyar: Multi-domain parallel computation of wake flows; ~~to appear in~~ Computer Methods in **174** (1999) Applied Mechanics and Engineering, ~~1999~~ 371-391.

[3] A.N. Brooks and T.J.R. Hughes: Streamline upwind/Petrov-Galerkin formulations for convection dominated flows with particular

emphasis on the incompressible Navier-Stokes equations; Computer Methods in Applied Mechanics and Engineering, vol.32 (1982) pp.199–259

[4] T.E. Tezduyar: Stabilized finite element formulations for incompressible flow computations; Advances in Applied Mechanics, vol.28 (1991) pp.1–44 ← (1992)

[5] Z. Johan, T.J.R. Hughes and F. Shakib: A globally convergent matrix-free algorithm for implicit time-marching schemes arising in finite element analysis in fluids; Computer Methods in Appl.Mech. Eng., vol.87 (1991) pp.281–304

[6] V. Kalro and T. Tezduyar: Parallel iterative computational methods for 3D finite element flow simulations; Computer Assisted Mechanics and Engineering Sciences, vol.5 (1998) pp.173–183

[7] Y. Saad and M. Schultz: GMRES: A generalized minimal residual algorithm for solving nonsymmetric linear systems; SIAM J. Sci. Statistical Computing, vol.7 (1986) pp.856–869

[8] A. Roshko: On the development of turbulent wakes from vortex street; NACA report 1191, NACA, (1954)

[9] C.H.K. Williamson: The existence of two stages in the transition to three-dimensionality of a circular cylinder wake; Physics of Fluids, vol.31 (1988) pp.3165–3167

[10] M. Coutanceau and J.R. Defaye: Circular cylinder wake configurations: a flow visualization survey; Applied Mechanics Rev, vol.44 (1991) pp.255–305

[11] George E. Karniadakis and George S. Triantafyllou: Three-dimensional dynamics and transition to turbulence in the wake of bluff bodies; J. Fluid Mechanics, vol.238 (1992) pp.1–30

[12] C.H.K. Williamson: Vortex dynamics in the cylinder wake; Annual Review of Fluid Mechanics, vol.28 (1996) pp.477–539

[13] V. Kalro and T.E. Tezduyar: Parallel 3D computation of unsteady flows around circular cylinder; Parallel Computing, vol.23 (1997) pp.1235–1248

[14] S. Taneda: Downstream development of the wakes behind cylinder; J. Phys. Soc. Jpn., vol.14 (1959) pp.843–848

[15] T. Matsui and M. Okude: Formation of the secondary vortex street in the wake of a circular cylinder; *Structure of Complex Turbulent Shear Flow*, (1983) pp.156–164

[16] J.M. Cimbala, H.M. Nagib and A. Roshko: Large structure in the far wakes of two-dimensional bluff bodies; J. Fluid Mechanics, vol.190 (1988) pp.265–298

[17] O. Inoue, T. Yamazaki and T. Bisaka: Numerical simulation of forced wakes around a cylinder; Int. J. Heat and Fluid Flow, vol.16 (1995) pp.327–332